

# The properties of the known QSOs astrometric solutions in Gaia DR2

Shilong Liao<sup>1,2</sup>, Zhaoxiang Qi<sup>1,2</sup>, Beatrice Bucciarelli<sup>3</sup>, Sufen Guo<sup>1,2</sup>, Zihuang Cao<sup>4</sup>, and Zhenghong Tang<sup>1,2</sup>

<sup>1</sup> Shanghai Astronomical Observatory, Chinese Academy of Sciences, 80 Nandan Road, Shanghai 200030, China  
e-mail: shilongliao@shao.ac.cn

<sup>2</sup> School of Astronomy and Space Science, University of Chinese Academy of Sciences, Beijing 100049, China

<sup>3</sup> INAF - Osservatorio Astrofisico di Torino, Strada Osservatorio, 2010025 Pino Torinese (TO), ITALY

<sup>4</sup> National Astronomical Observatory, Chinese Academy of Sciences, 20A Datun Road, Chaoyang District, Beijing, China

Received Month day, 2018; accepted Month day, 2018

## ABSTRACT

**Aims.** The second release of Gaia Release 2 (Gaia DR2) contains the astrometric parameters for more than half a million quasars after cross matching with the prototype of the upcoming ICRF3 and the AllWISE AGN catalog. These quasars are used to define and materialize a kinematically non-rotating reference frame in optical band and to estimate the systematics in the parallaxes. We aim to evaluate the properties of the QSOs astrometric solution.

**Methods.** Besides the QSOs from the AllWISE AGN catalog, we cross match the QSOs sample from LQAC3, SDSS DRQ14 and LAMOST DR5 with the Gaia DR2 to create the largest quasar sample. The final sample (designated as Known Quasars Catalog for Gaia mission, KQCG) contains 779349 objects. With this largest QSOs sample, we estimate the global bias in parallax and proper motion, analysis the proper motion field with the vector spherical harmonics (VSH) functions and compare with different QSOs subsets. The parallaxes are expanded with the scalar spherical harmonics. And finally we carry out the positional comparison between the ICRF2 sources and their counterparts in Gaia DR2.

**Results.** The mean global parallaxes bias for the KQCG quasars is  $-0.0308$  mas, and the median parallax is  $-0.0283$  mas. The roughly quadratic variation with  $\sim 0.010$  mas smaller parallaxes towards the ecliptic poles does not show in KQCG sample. The VSH analysis result of KQCG shows a different rotation compared with the Gaia-CRF2 sample in the proper motion field. The rotations of different samples are not larger than  $10\mu\text{as/yr}$  for each axis. The glide vector of KQCG is around  $(-8, +10, +9) \pm 2.5\mu\text{as/yr}$ . There is a  $\sim +0.01$  mas/yr bias in the declination direction of proper motion, and the typical glide of the proper motion field is  $(-9, 8, 0) \pm 2\mu\text{as/yr}$  after subtracting the bias in  $\mu_\delta$ . The quasars sample used to define the Gaia reference frame shows a different rotation in northern  $((2.2, 2.8, -1.5) \pm 2.0\mu\text{as/yr})$  and southern  $((9.5, 8.7, 0.8) \pm 2.3\mu\text{as/yr})$  hemisphere. The scalar harmonics spherical expansion show a significant RMS value about  $23\mu\text{as}$  for the harmonic degree  $l = 4$ . No significant rotation is found between ICRF2 sources and their counterparts in Gaia DR2.

**Key words.** reference frame – parallax bias – proper motions – quasars

## 1. Introduction

The second Gaia data release (Gaia DR2) contains results for 1.693 billion sources from magnitude 3 to 21 based on the observations of the European Space Agency Gaia satellite during the period of 22 months between 2014 July 25 and 2016 May 23 (Lindgren (2018), hereafter denoted as Gaia-DR2 Astrometric paper). 1332 millions sources are provided with five astrometric parameters (positions, parallaxes, and proper motions). An additional 361 million sources, mostly faint sources, are provided with approximate positions at the reference epoch J2015.5. For the sources with five-parameter astrometric solutions, the median uncertainty in parallax and position at the reference epoch J2015.5 is about 0.04 mas for bright ( $G < 14$  mag) sources, 0.1 mas at  $G = 17$  mag, and 0.7 mas at  $G = 20$  mag. In the proper motion components, the corresponding uncertainties are 0.05, 0.2, and 1.2 mas  $\text{yr}^{-1}$ , respectively (Lindgren (2018)).

Quasars (quasi-stellar objects or QSOs) are extremely distant and small in apparent size. They are ideal objects in establishing reference frame since they present no significant parallax

or proper motion. Among of the astrometric solution, Gaia DR2 provides more than 550 000 quasars, obtained from a positional cross-match with the ICRF3-prototype and AllWISE AGN catalogues, with complete five astrometric parameters - positions, parallaxes, and proper motions (Lindgren (2018)). With these half a million quasars, a kinematically non-rotating reference frame (the celestial reference frame of Gaia DR2, Gaia-CRF2) in the optical domain is defined (Mignard (2018), hereafter in denote as Gaia-CRF2 paper). The optical positions for 2843 sources in common with the unpublished ICRF3-prototype with accurate VLBI positions are used to align the axes of Gaia-CRF2 with the ICRF radio frame. From these quasars and validation solutions, the systematics in the parallaxes depending on position, magnitude, and colour are estimated with a value below 0.1 mas. Besides, there is an overall negative bias of about 0.03 mas (Lindgren (2018)).

However, besides QSOs from the ALLWISE AGN catalog (Secrest (2015)), there are other QSO catalogues that can enlarge the sample of known quasars in Gaia DR2. To maximize the number of known QSOs/AGNS, in addition to the QSOs

from AllWISE, we choose three samples for their huge number of reliable QSOs/AGNs. We started from the third Large Quasar Astrometric Catalogue (LQAC3) (Souhay (2015)) QSOs list. LQAC3 contains all the known QSOs discovered in 2dF/2QZ survey (Croom (2004)), the DR10Q of the SDSS-III (Bolton (2012); Pâris (2014)) and the VLBI QSOs listed in ICRF2, VLBA, VLA, and JVAS catalogs. And also the quasars from Hewitt & Burbidge catalog (Hewitt (1993)) and Véron-Cetty & Véron catalog (Véron (2010)). Here in this compilation, the QSOs from SDSS in LQAC3 will be updated with the latest spectroscopically confirmed QSOs in the SDSS- DR14 Quasar Catalog (DR14Q) by using data from the Baryon Oscillation Spectroscopic Survey (BOSS; Eisenstein (2015)) and photometrically selected QSO in SDSS (Pâris (2017)). And then enter the spectroscopically confirmed QSOs in LAMOST DR5 (see <http://dr5.lamost.org> for more detail) using LAMOST spectroscopic data (Cui (2012)). All these QSOs have been compiled into a catalog called Known QSOs catalog for the Gaia mission (KQCG, Liao (2018)), which contains 1843850 objects.

This work aims to provide an overall analysis of the QSOs sources in Gaia DR2. We begin with the global parallaxes bias analysis in section 3 after the selection of the quasars sample in section 2. In section 4, we implement the vector spherical harmonics analysis of the selection quasars and compare to other samples. The scalar spherical harmonics analysis of the parallaxes is presented in section 5, with the comparison of the ICRF2 sources and their counterparts in Gaia DR2 followed in section 6. The last section is the conclusion and discussion.

## 2. Selection of quasars

To find the known QSO sources in Gaia DR2 astrometric solutions, we use the following joint conditions as adopted by the Gaia DR2 astrometric paper (Lindgren (2018)) to reduce the risk of contamination by the stars:

- (i)  $\text{astrometric\_matched\_observations} \geq 8$ ,
- (ii)  $\text{astrometric\_params\_solved} = 31$ ,
- (iii)  $|(\omega + 0.029\text{mas})/\sigma_\omega| < 5$ ,
- (iv)  $(\mu_{\alpha^*}/\sigma_{\mu_{\alpha^*}})^2 + (\mu_{\delta^*}/\sigma_{\mu_{\delta^*}})^2 < 25$ ,
- (v)  $|\sin b| > 0.1$
- (vi)  $\rho < (2 \text{ arcsec}) \times |\sin b|$

Where  $\rho$  is the radius for the positional matching,  $b$  is the Galactic latitude. Under these conditions, 779349 QSO sources are found in the Gaia DR2 sources (denoted as KQCG in the rest of this paper). Among of them, 555934 sources are already found in the Gaia DR2 astrometric paper, which means that 223415 additional known QSOs are found. See the Figure 1 and 2 for the sky density distribution. The G magnitude histogram of the KQCG quasars is showed in Figure 3, most of the 223415 additional QSOs are fainter than magnitude 19. The distribution of the parallaxes and the proper motions of these additional sources can be found in Figure 4 and Figure 5.

## 3. Global bias analysis

### 3.1. Parallax bias analysis

QSOs are ideal objects to check the parallax zero point since they present no significant parallax. The parallaxes for the whole KQCG QSOs sample versus magnitude and colour are showed in figure 6. The mean and the median parallax of the KQCG sample is  $-0.0308 \text{ mas}$  and  $-0.0283 \text{ mas}$ , respectively. For the high-precision subset ( $\sigma_\omega < 1 \text{ mas}$ , 650232 objects), the corresponding

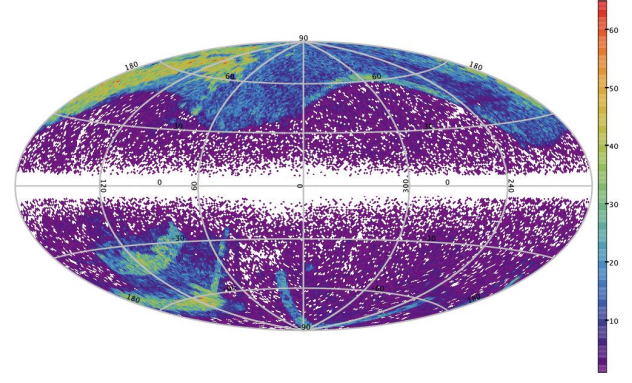


**Fig. 1.** The sky distribution of the 223415 extra KQCG known QSOs found in Gaia DR2 sources. The map shows the sky density with each cell of approximately  $0.84 \text{ deg}^2$ , using the Hammer-Aitoff projection in Galactic coordinates with zero longitude at the centre and increasing longitude from right to left.

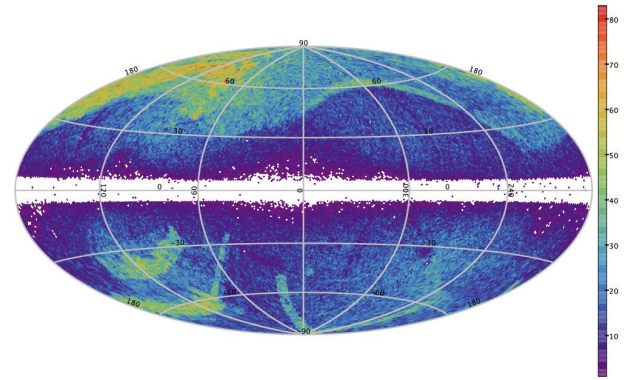


**Fig. 2.** The sky distribution of the total 779349 KQCG known QSOs found in Gaia DR2 sources. The map shows the sky density with each cell of approximately  $0.84 \text{ deg}^2$ , using the Hammer-Aitoff projection in Galactic coordinates with zero longitude at the centre and increasing longitude from right to left.

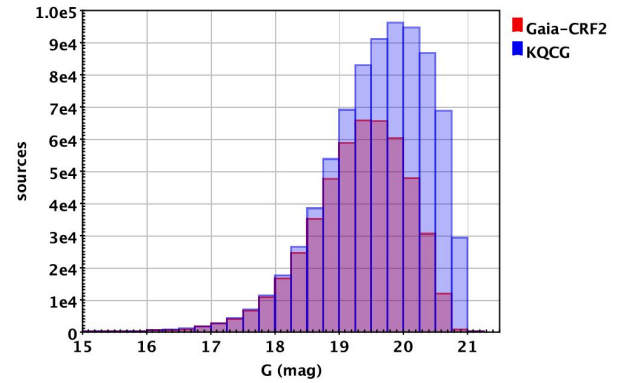


**Fig. 3.** G magnitude distribution of the Gaia-CRF2 sources and the KQCG sources.

values are  $-0.0278 \text{ mas}$  and  $-0.0277 \text{ mas}$ . These value agree with the results in Gaia-DR2 Astrometric paper (Lindgren (2018)). In the top panel of Figure 7, the parallax against ecliptic latitude does not show the roughly quadratic variation with  $\sim 0.01 \text{ mas}$  smaller towards the ecliptic poles as found in the Gaia-DR2 Astrometric paper (Lindgren (2018)). We plot the magnitude distribution of the KQCG quasars sample versus the Ecliptic latitude in the bottom panel of Figure 7, and find that the magnitude

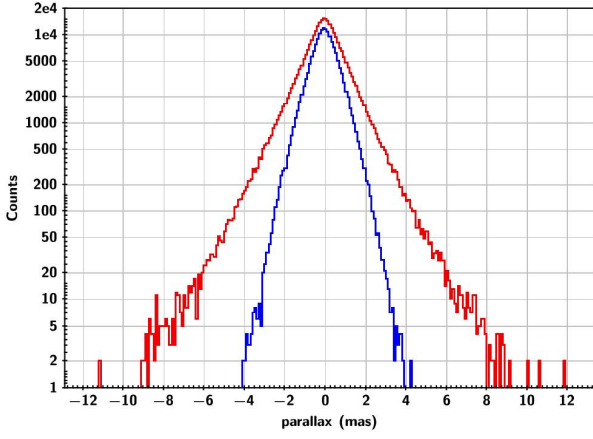


**Fig. 4.** Parallax distribution for 223415 extra known QSOs from KQCG sources. Outer (red) curve is the whole 223415 sample; Inner (blue) is the subsample of 166122 sources with  $\sigma_\omega < 1$  mas.

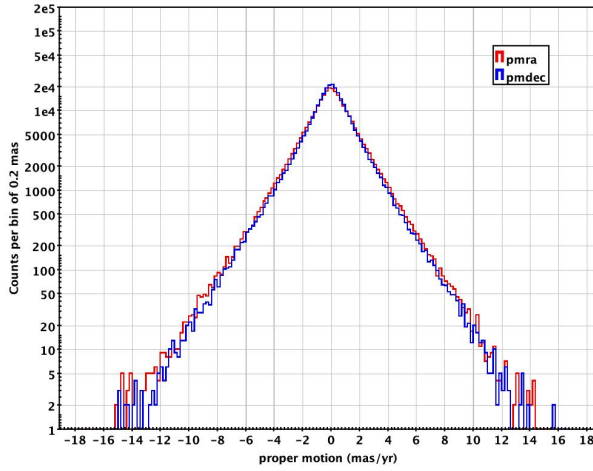


**Fig. 5.** Proper motion distribution for 223415 extra known QSOs from KQCG sources. The red curve is the proper motion in right ascension (pmra) and the blue is the proper motion in declination (pmdec).

median is quiet stable ( $\sim 19.7$  G). We believe the quadratic variation with  $\sim 0.01$  mas found in the Gaia-DR2 astrometric paper is caused by the sources around the ecliptic poles are fainter in general, see Figure 9 for the magnitude sky distribution. We also plot the parallax against the Galactic longitude, see Figure 8, the median magnitude varies half magnitude versus Galactic longitude. With the brighter median magnitude, the parallax bias is larger in depletion zones at  $[320^\circ, 360^\circ]$  and  $[0^\circ, 10^\circ]$ .

### 3.2. Proper motion bias analysis

QSOs are extremely distant objects. Besides parallaxes, the proper motions of quasars are nominally zero for the quasars selected for the reference frame (the Galactic acceleration effect is neglected here). In this section, we try to perform the global statistics to investigate their global quality. We plot the distribution of the proper motion versus the magnitude and the effective wavenumber of two quasars sample: KQCG and those quasars used for the frame rotation (they are denoted as Type2+Type3, see section 4.). The mean and median parallax of the KQCG sample is  $-1.2 \mu\text{as/yr}$  and  $-2.4 \mu\text{as/yr}$  in right ascension direction,  $+10.4 \mu\text{as/yr}$  and  $+11.3 \mu\text{as/yr}$  in declination direction, respectively. For Type2+Type3 sample, the result is  $-0.4 \mu\text{as/yr}$

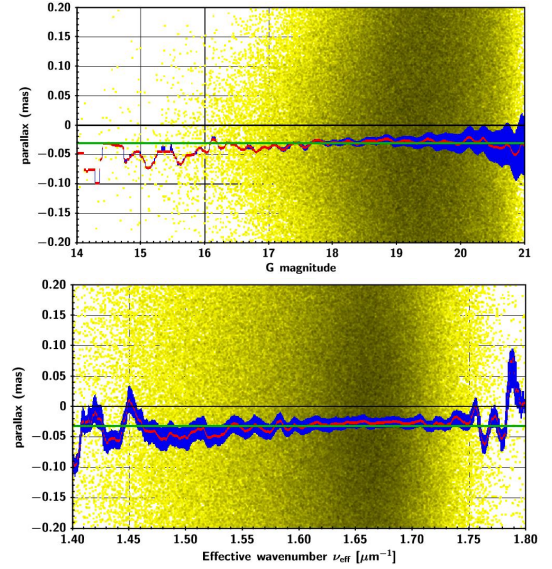


**Fig. 6.** Parallaxes for the all KQCG QSOs plotted against Gaia G magnitude (top), colour (bottom). As adopted by the Gaia-DR2 Astrometric paper (Lindegren (2018)), only the scale between  $[-0.2, 0.2]$  mas is plotted. The yellow dots are the parallax data points, the black lines are the zero parallax values, the green lines are the  $-0.0308$  mas mean parallax for the full KQCG sample, while the red lines are the parallax medians  $\omega_{med}$  of each running-bin, the blue curves represent the interval of  $[0.98\omega_{med}, 1.02\omega_{med}]$ . The same apply hereafter in.

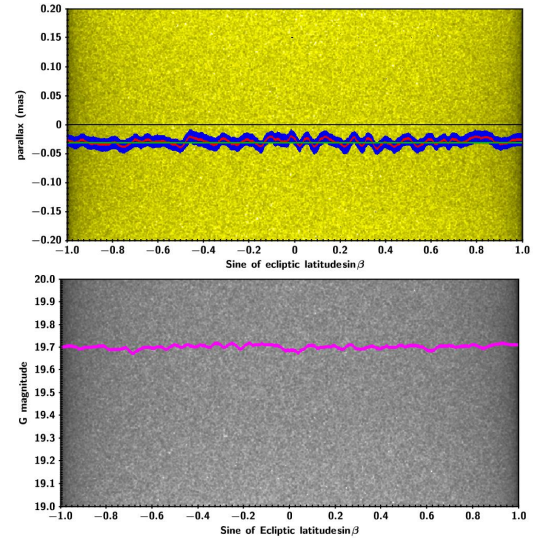


**Fig. 7.** Parallaxes for the KQCG QSOs plotted against ecliptic latitude (top) and the Gaia G magnitude plotted against the ecliptic latitude (bottom). In the top panel, the yellow dots are the parallax data points, the black line represents the zero parallax value, the green line is the  $-0.0308$  mas mean parallax for the full KQCG sample, while the red lines are the parallax  $\omega_{med}$  medians of each running bin, the blue curves represent the interval of  $[0.98\omega_{med}, 1.02\omega_{med}]$ . In the bottom panel, the gray dots are the magnitude data points, only the scale  $[19, 20]$  for G magnitude are plotted. The pink line is the magnitude median of the running-bin.

and  $-1.3 \mu\text{as/yr}$  in right ascension direction,  $+12.0 \mu\text{as/yr}$  and  $+11.7 \mu\text{as/yr}$  in declination direction. See Figure 10 and Figure 11 for the proper motion versus magnitude and colour. There is a proper motion bias of  $+10 \mu\text{as/yr}$  level in declination direction.



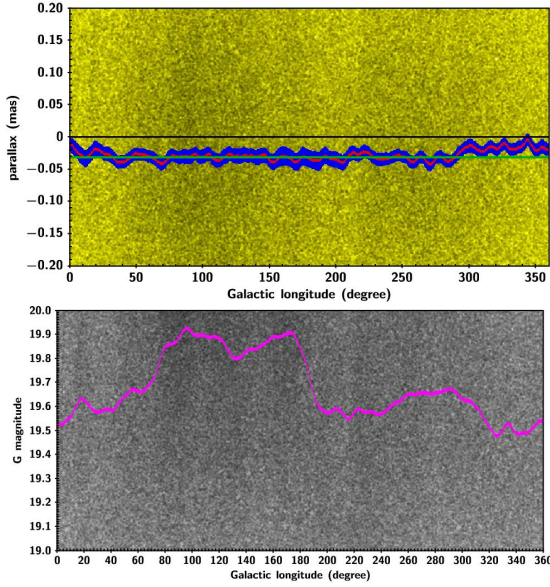


**Fig. 8.** Parallaxes for the all KQCG QSOs plotted against galactic longitude (top) and the Gaia G magnitude plotted against the galactic longitude (bottom). In the top panel, the yellow dots are the parallax data points, the black line represents the zero parallax value, the green line is the  $-0.0308$  mas mean parallax for the full KQCG sample, while the red lines are the parallax medians  $\omega_{med}$  of each running-bin, the blue curves represent the interval of  $[0.98\omega_{med}, 1.02\omega_{med}]$ . In the bottom panel, the gray dots are the magnitude data points, only the scale between  $[19, 20]$  for G magnitude are plotted. The pink line is the magnitude median of each running-bin.

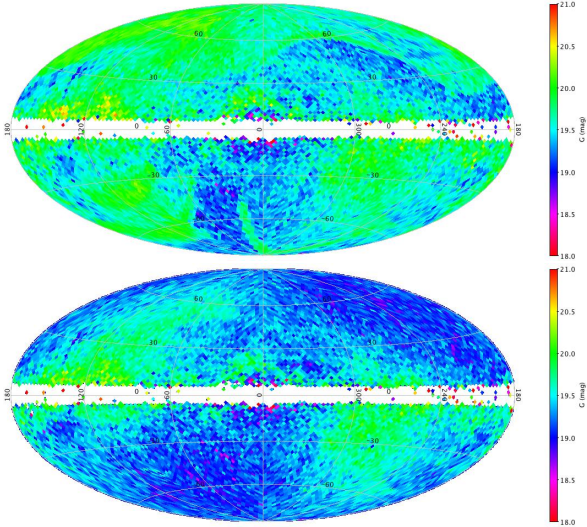


**Fig. 9.** Spatial distribution of the magnitude of the KQCG (top) and Gaia-CRF2 (bottom) sample in Galactic coordinates. This map is in Aitoff projection with Galactic longitude zero at the center and increasing from left to right. Median values are computed in cells of approximately  $3.357\text{deg}^2$ . Sources around the ecliptic poles are fainter than other regions of Gaia-CRF2 sample.

#### 4. Vector spherical harmonics analysis of the proper motion field

In this section, we perform the vector spherical harmonics (VSH) expansion of the KQCG QSOs sample. The spatial distribution of the proper motion vector field is shown in Figure 12. The VSH model explained in Mignard & Klioner (Mignard (2012))

is adopted. To have a better comparison of the expansion results, five groups are investigated: the KQCG QSO sample (denoted as KQCG), the Gaia-CRF2 QSO sample (denoted as GCRF2), the 489163 AllWISE AGN indicated in the Gaia Archive by the field *frame\_rotator\_object\_type* = 3 (denoted as Type3 here) used to determine the kinematically non-rotating celestial frame, and 2843 sources matched to the ICRF3 prototype and indicated by *frame\_rotator\_object\_type* = 2 (denoted as Type2 here) and the combination of Type2 and Type3 (denoted as Type2+Type3).

The results of the VSH analysis are listed in table 1. The rotation of the KQCG sample change from about  $10\mu\text{as/yr}$  with the harmonics of degree  $l = 1$  to a few  $\mu\text{as/yr}$  with  $l = 5$  may caused by the not uniform spatial distribution of the KQCG quasars sample. The rotation result of KQCG agrees with the result of Type2+Type3 sample, although a larger value in y component. While the GCRF2 sample result shows a very different rotation, especially in x and y component. The faint end ( $G \geq 19$ ) and the bright end ( $G < 19$ ) of KQCG sample show a very different rotation (especially x and y component), this is consistent with the GCRF2 and the Type2+Type3 sample. With the much less number, the VSH analysis result of Type2 sample does not show any significant signal as the other sample. Even though the rotation results of different sample vary from each other, the rotations of them are not larger than  $10\mu\text{as/yr}$  for each axis.

The glide vector of KQCG is  $(-8.7 \pm 2.9, +9.6 \pm 2.3, +8.9 \pm 2.7)\mu\text{as/yr}$ . This result agrees with the other sample, especially in x and z component, with the y component of the GCRF2 sample relatively smaller. As found in the 3.2, there is a global bias in  $\mu_\delta$ , if we subtract the bias in  $\mu_\delta$  (that is  $\mu_\delta - \bar{\mu}_\delta$ ) before performing the VSH analysis, the glide in z axis can be treated as 0 within the error, see the rows indicated by \* in table 1.

If we consider only the rotation, then we have:

$$\begin{aligned} \mu_{\alpha*} &= -w_X \cos \alpha \sin \delta - w_Y \sin \alpha \sin \delta + w_Z \cos \delta \\ \mu_\delta &= +w_X \sin \alpha - w_Y \cos \alpha \end{aligned} \quad (1)$$

We use this equation to further investigate the sources of KQCG and Type2+Type3 in Northern and Southern hemisphere, respectively. The results are shown in table 2. For the Type2 sample, no significant rotation is found. For Type2+Type3 quasar sample, the rotation in southern hemisphere is more significant than the northern hemisphere in x and y component. For KQCG sample, the rotation of x and y component agrees with northern and southern hemisphere, while the z component is more significant in northern hemisphere.

If we try to estimate the proper motion bias in declination (denoted as  $d\mu_\delta$  here), an additional term should be added in Equation (1):

$$\begin{aligned} \mu_{\alpha*} &= -w_X \cos \alpha \sin \delta - w_Y \sin \alpha \sin \delta + w_Z \cos \delta \\ \mu_\delta &= +w_X \sin \alpha - w_Y \cos \alpha + d\mu_\delta \end{aligned} \quad (2)$$

The results can be found in table 2. The estimated bias in  $\mu_\delta$  is consistent within error between these two quasars samples.

#### 5. The scalar field of parallaxes

As the parallaxes of the quasars are small enough to be treated as zero, their parallaxes can be treated as residuals. The parallaxes of the quasars can be seen as the radial part of the spatial positions differences on the celestial sphere, see Figure 13 for the parallax sky distribution of KQCG sample. Here in this section, we try to analysis the parallax residuals using the scalar spherical

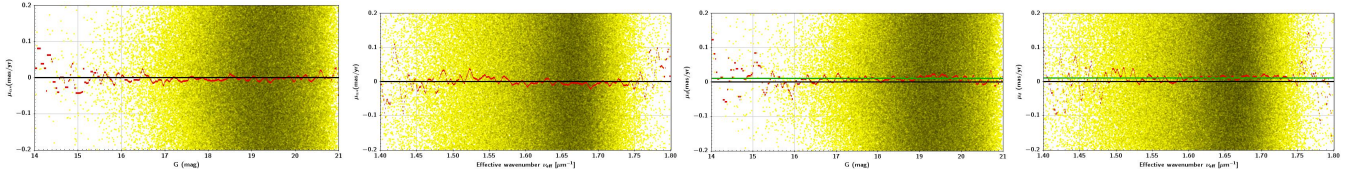


**Fig. 10.** Proper motion for the all KQCG QSOs plotted against the Gaia G magnitude and colour (The first and second figure from left is the  $\mu_{\alpha^*}$ , and the third and fourth is for  $\mu_{\delta}$ ). The yellow dots are the proper motion data. The black line represents the zero value, the green lines in the two figures on the right is the  $+10.4 \mu\text{as/yr}$  mean  $\mu_{\delta}$ , while the red lines are the proper motion medians  $\mu_{med}$  in each direction of each running-bin.

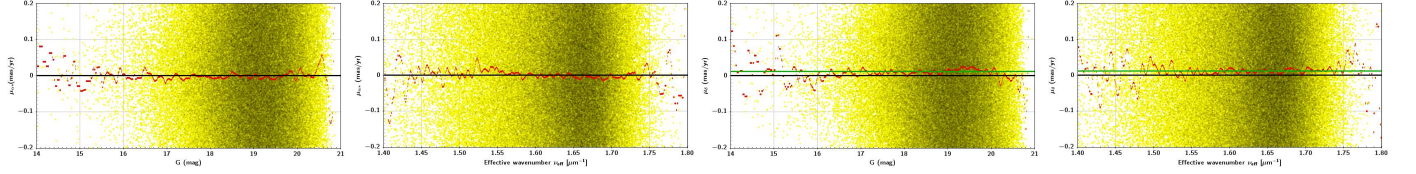


**Fig. 11.** Proper motion for the all Type2+Type3 QSOs plotted against the Gaia G magnitude and colour (The first and second figure from left is the  $\mu_{\alpha^*}$ , and the third and fourth is for  $\mu_{\delta}$ ). The yellow dots are the proper motion data. The black line represents the zero value, the green lines in the two figures on the right is the  $+12.0 \mu\text{as/yr}$  mean  $\mu_{\delta}$ , while the red lines are the proper motion medians  $\mu_{med}$  in each direction of each running-bin.

**Table 1.** VSH analysis of the proper motion field of different quasars sample in Gaia DR2. The VSH analysis results of GCRF2 sample (the last four rows) are taken from the Table 2 of the Gaia-CRF2 paper. The number of Type 3 sample is less than 489163 is because there are 3178 of them do not contain the parallax solution. The row \* means the bias in  $\mu_{\delta}$  is subtracted (that is  $\mu_{\delta} = \mu_{\delta} - \bar{\mu}_{\delta}$ ) when performing the VSH analysis.

Source Subset	$l_{max}$	N	Rotation [ $\mu\text{as/yr}$ ]			Glide [ $\mu\text{as/yr}$ ]		
			x	y	z	x	y	z
KQCG	1	779349	$12.8 \pm 2.0$	$11.5 \pm 1.7$	$-3.9 \pm 2.1$	$-7.3 \pm 2.1$	$10.2 \pm 1.9$	$12.0 \pm 2.1$
	5	779349	$1.9 \pm 2.6$	$6.5 \pm 2.2$	$6.7 \pm 2.7$	$-8.7 \pm 2.9$	$9.6 \pm 2.3$	$8.9 \pm 2.7$
	*	779349	$1.9 \pm 2.6$	$6.5 \pm 2.2$	$6.7 \pm 2.7$	$-8.6 \pm 2.9$	$9.6 \pm 2.3$	$-3.3 \pm 2.7$
$G \geq 19$	1	615496	$16.2 \pm 2.5$	$15.7 \pm 2.2$	$-4.5 \pm 2.6$	$-7.6 \pm 2.7$	$10.9 \pm 2.4$	$10.1 \pm 2.6$
	5	615496	$3.5 \pm 3.4$	$11.2 \pm 2.8$	$7.8 \pm 3.5$	$-8.4 \pm 3.8$	$10.0 \pm 2.9$	$6.5 \pm 3.5$
$G < 19$	1	163853	$1.1 \pm 1.5$	$-3.7 \pm 1.3$	$-2.3 \pm 1.5$	$-9.5 \pm 1.6$	$9.4 \pm 1.4$	$18.1 \pm 1.5$
	5	163853	$-2.3 \pm 2.0$	$-8.6 \pm 1.7$	$2.4 \pm 1.9$	$-11.8 \pm 2.2$	$8.0 \pm 1.7$	$15.3 \pm 1.9$
Type2+Type3	1	488828	$5.4 \pm 1.6$	$5.0 \pm 1.5$	$-0.2 \pm 1.8$	$-9.2 \pm 1.7$	$6.6 \pm 1.6$	$16.4 \pm 1.8$
	5	488828	$2.0 \pm 1.9$	$1.9 \pm 1.7$	$6.3 \pm 2.1$	$-9.2 \pm 2.2$	$8.5 \pm 1.8$	$13.7 \pm 2.1$
	*	488828	$2.0 \pm 2.0$	$1.9 \pm 1.7$	$6.4 \pm 2.1$	$-9.1 \pm 2.2$	$8.5 \pm 1.8$	$-0.4 \pm 2.1$
$G \geq 19$	1	363558	$7.2 \pm 2.0$	$8.3 \pm 1.9$	$-0.5 \pm 2.3$	$-8.8 \pm 2.1$	$5.5 \pm 2.1$	$16.2 \pm 2.3$
	5	363558	$3.5 \pm 2.5$	$6.6 \pm 2.2$	$5.5 \pm 2.7$	$-8.8 \pm 2.8$	$8.0 \pm 2.3$	$14.2 \pm 2.7$
$G < 19$	1	125270	$0.3 \pm 1.7$	$-4.2 \pm 1.5$	$-0.1 \pm 1.8$	$-11.0 \pm 1.9$	$9.7 \pm 1.7$	$17.7 \pm 1.8$
	5	125270	$-0.1 \pm 2.3$	$-8.3 \pm 1.9$	$5.6 \pm 2.4$	$-10.9 \pm 2.6$	$10.2 \pm 2.1$	$14.3 \pm 2.4$
Type3	1	485985	$5.4 \pm 1.6$	$4.8 \pm 1.5$	$-0.3 \pm 1.8$	$-9.1 \pm 1.7$	$6.6 \pm 1.6$	$16.3 \pm 1.8$
	5	485985	$2.0 \pm 1.9$	$1.6 \pm 1.7$	$6.4 \pm 2.1$	$-9.2 \pm 2.2$	$8.6 \pm 1.8$	$13.6 \pm 2.1$
Type2	1	2843	$-5.7 \pm 20.9$	$27.5 \pm 19.6$	$14.2 \pm 40.5$	$-10.5 \pm 30.6$	$1.5 \pm 30.1$	$32.2 \pm 40.5$
	5	2843	$28.6 \pm 29.2$	$36.0 \pm 29.3$	$13.7 \pm 43.2$	$-10.5 \pm 41.2$	$20.0 \pm 38.1$	$30.0 \pm 43.2$
GCRF2	1	556869	$-3.6 \pm 0.8$	$-2.2 \pm 0.7$	$-0.9 \pm 0.9$	$-7.0 \pm 0.8$	$4.7 \pm 0.7$	$12.1 \pm 0.7$
	5	556869	$-5.5 \pm 1.1$	$-7.4 \pm 0.9$	$5.6 \pm 1.2$	$-9.2 \pm 1.2$	$4.7 \pm 1.0$	$11.6 \pm 1.0$
$G > 19$ $G < 19, \mu < 2 \text{ mas/yr}$	5	406356	$9.8 \pm 2.1$	$6.2 \pm 1.8$	$7.0 \pm 2.4$	$-8.3 \pm 2.3$	$3.3 \pm 1.9$	$15.6 \pm 1.9$
	5	149146	$-11.2 \pm 1.3$	$-12.0 \pm 1.1$	$4.4 \pm 1.4$	$-9.8 \pm 1.5$	$4.6 \pm 1.2$	$10.4 \pm 1.1$



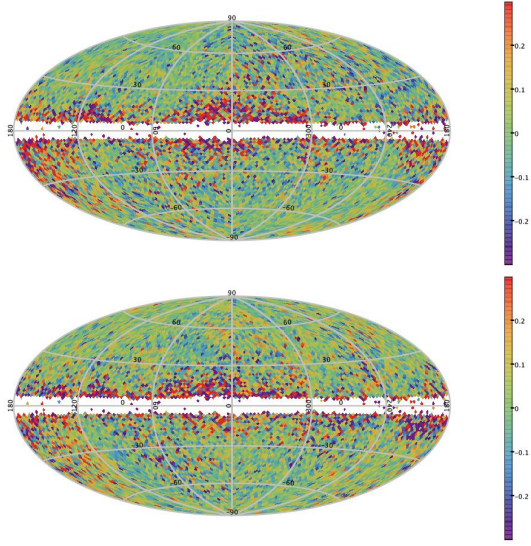


**Fig. 12.** Spatial distribution of the proper motion of the KQCG sample in Galactic coordinates. This map is in Aitoff projection with Galactic longitude zero at the center and increasing from left to right. Median values are computed in cells of approximately  $3.357\text{deg}^2$ .

**Table 2.** Global rotation from the KQCG, Type2 and Type3 quasars. "-" means no estimation.

Subset	$w_X$ ( $\mu\text{as/yr}$ )	$w_Y$ ( $\mu\text{as/yr}$ )	$w_Z$ ( $\mu\text{as/yr}$ )	$d\mu_\delta$ ( $\mu\text{as/yr}$ )
Type2	$-4\pm 20$	$28\pm 19$	$14\pm 40$	-
North	$0\pm 29$	$21\pm 27$	$30\pm 35$	-
South	$4\pm 32$	$35\pm 30$	$-4\pm 60$	-
Type2+Type3	$5.8\pm 1.6$	$5.3\pm 1.5$	$-0.3\pm 1.8$	-
North	$5.3\pm 1.6$	$4.8\pm 1.5$	$-0.2\pm 1.8$	$11.7\pm 1.2$
South	$2.2\pm 2.2$	$2.8\pm 2.0$	$-1.5\pm 2.5$	-
	$5.2\pm 2.2$	$-1.5\pm 2.1$	$-1.5\pm 2.5$	$15.2\pm 4.0$
	$9.5\pm 2.3$	$8.7\pm 2.2$	$0.8\pm 2.3$	-
	$7.0\pm 2.4$	$10.7\pm 2.2$	$0.8\pm 2.3$	$10.1\pm 1.9$
KQCG	$11.5\pm 1.9$	$11.4\pm 1.7$	$-4.4\pm 2.1$	-
	$11.0\pm 2.0$	$10.1\pm 1.7$	$-4.3\pm 2.1$	$9.2\pm 1.4$
North	$8.1\pm 2.6$	$10.5\pm 2.2$	$-8.0\pm 2.8$	-
	$9.2\pm 2.6$	$6.3\pm 2.4$	$-8.1\pm 2.8$	$10.9\pm 2.0$
South	$15.8\pm 3.1$	$13.4\pm 2.7$	$1.3\pm 2.8$	-
	$13.7\pm 3.1$	$15.4\pm 2.8$	$1.3\pm 2.8$	$8.6\pm 2.5$

harmonics as follows (Bucciarelli (2011)):

$$V_\pi(\alpha, \delta) = \Delta\pi = \sum_l \sum_{m=-l}^l c_{lm} Y_{lm}(\alpha, \delta) \quad (3)$$

Where  $Y_{lm}$  are the standard spherical functions defined here the following sign convention:

$$Y_{lm} = (-1)^m \sqrt{\frac{2l+1}{4\pi} \frac{(l-m)!}{(l+m)!}} P_{lm}(\sin \delta) e^{im\alpha} \quad (4)$$

for  $m \geq 0$  and we have  $Y_{l,-m}(\alpha, \delta) = (-1)^m Y_{lm}^*(\alpha, \delta)$  for  $m < 0$ . The  $*$  denotes complex conjugation.  $P_{lm}(x)$  is the associated Legendre functions.

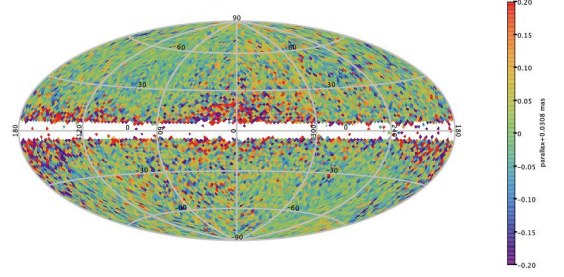


**Fig. 13.** Spatial distribution of the parallaxes of the KQCG sample in Galactic coordinates. This map is in Aitoff projection with Galactic longitude zero at the center and increasing from left to right. Median values are computed in cells of approximately  $3.357\text{deg}^2$ .

**Table 3.** The scalar spherical harmonics expansion of the parallaxes of the quasars sample.

$l$	Type2+Type3		KQCG	
	$P_l^{1/2}(\mu\text{as})$	$Z_{\chi^2}$	$P_l^{1/2}(\mu\text{as})$	$Z_{\chi^2}$
1	17.5	6.06	15.7	5.57
2	10.8	3.22	12.3	4.09
3	16.3	5.09	15.9	5.12
4	23.8	7.98	21.8	7.48
5	14.7	4.01	15.3	4.54
6	12.2	2.41	11.2	2.05
7	14.1	3.63	14.7	4.23
8	10.9	1.44	10.6	1.47
9	11.6	2.60	10.4	2.12
10	12.8	3.12	13.1	3.71

The equation 3 can be reduced as:

$$\Delta\pi = \sum_{l=1}^{l_{\max}} \left[ c_{l0}^R Y_{l0}^R + 2 \sum_{m=1}^l (c_{lm}^R Y_{lm}^R - c_{lm}^I Y_{lm}^I) \right] \quad (5)$$

Where  $R$  and  $I$  denote the real and imaginary part of the function. The power of the expansion of different degree  $l$  is defined as follows:

$$P_l = (c_{l0}^R)^2 + 2 \sum_{m=1}^l [(c_{lm}^R)^2 + (c_{lm}^I)^2] \quad (6)$$

The significant of a harmonic degree  $l$  is calculated by the equation (83) and (84) from the Mignard & Klioner (2012) paper. The analysis results of the parallaxes in the Type2+Type3 sample and the KQCG sample can be found in table 5. Both two samples show a significant harmonic level of degree 4 ( $P_{l=4}^{1/2}$  around  $23\mu\text{as}$ ), which corresponds to an angular scale  $\sim 180^\circ/l=45^\circ$ .

## 6. Comparison of the optical and the ICRF2 radio positions

The ICRF2 catalog was computed using nearly 30 years of VLBI observations and provides accurate positions of 295 “defining” sources and generally less accurate positions of 3119 other radio sources, leading to 3414 sources in total (Fey (2015)), see Figure 14 for the sky distribution. In this section, we try to compare the angular differences in Gaia DR2 and the ICRF2 sources.

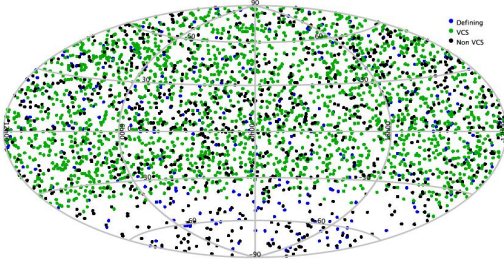


**Fig. 14.** ICRF2 sources sky distribution, Hammer-Aitoff projection in Equatorial coordinates. The blue dots are the 295 defining sources, while the green dots are the 2197 Very long baseline array calibrator survey (VCS) sources, and the 922 black are the non VCS sources. All defining sources are also non-VCS sources.

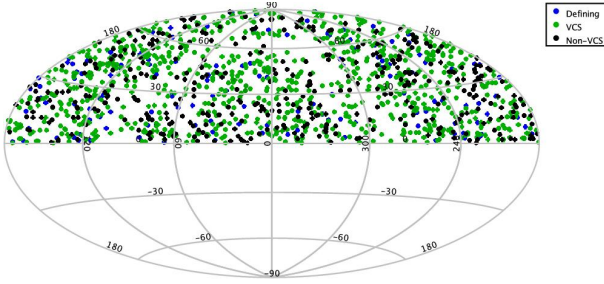


**Fig. 15.** Sky distribution of ICRF2 sources counterparts found in Gaia DR2, Hammer-Aitoff projection in Equatorial coordinates. The blue dots are the defining sources, while the green dots are the Very long baseline array calibrator survey (VCS) sources, and the blacks are the non VCS sources.

### 6.1. Identification of ICRF2 sources in Gaia DR2

To find the counterparts of the ICRF2 sources in Gaia DR2 astrometric solutions, we use the following joint conditions as adopted by the Gaia-DR2 Astrometric paper:

- (i)  $\rho \leq 100\text{mas}$ ,
- (ii)  $\text{astrometric\_matched\_observations} \geq 8$ ,
- (iii)  $\sigma_\omega < 1\text{ mas}$ ,
- (iv)  $|\omega/\sigma_\omega| < 5$ ,
- (v)  $(\mu_{\alpha^*}/\sigma_{\mu_{\alpha^*}})^2 + (\mu_{\delta^*}/\sigma_{\mu_{\delta^*}})^2 < 25$ .

Where  $\rho$  is the radius for the positional matching. Under these conditions, 1321 ICRF2 sources are found in the Gaia DR2 sources see Figure 15 for the sky density. One can see that all the matched ICRF2 sources are in the northern hemisphere. The most likely explanation might be that the position errors of the sources in southern hemisphere are generally substantially worse due to small number of observation stations in the southern hemisphere (Malkin (2015)).

The angular distance between two objects is computed as:

$$\rho = (\Delta\alpha_*^2 + \Delta\delta^2)^{1/2} \quad (7)$$

Where  $\Delta\alpha_* = \Delta\alpha \cos \delta$ . Figure 16 gives the histogram of the angular differences. Among the matched sources, most of the angular differences are smaller than 1 mas, and also a few sources with  $\rho$  larger than 10 mas.

Figure 17 shows the angular differences  $\rho$  between the ICRF2 sources and their counterparts in Gaia DR2 with respect to the formal positional uncertainties  $\sigma_{\text{pos,max}}$  of the ICRF2 sources and the Gaia DR2 sources. Most of the sources in Gaia

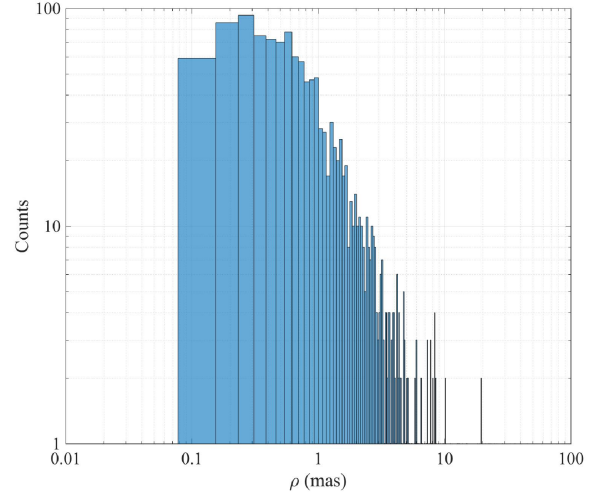


**Fig. 16.** Histogram of the angular differences  $\rho$  between Gaia DR2 and ICRF2 sources for 1321 common sources. The axis is log-log scale, and the bins in  $\rho$  is 0.07735 mas.

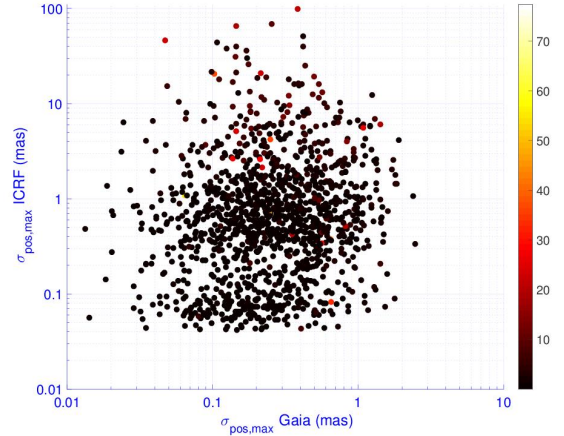


**Fig. 17.** The formal position uncertainties  $\sigma_{\text{pos,max}}$  of the Gaia DR2 sources (abscissa) with respect to the ICRF2 sources (ordinate). The color bar on the right is the position differences  $\rho$  (in mas) between Gaia DR2 and the ICRF2 sources. The axis is log-log scale.

DR2 have a position uncertainty under 1 mas, while the uncertainties of the sources in ICRF2 range from 0.04mas to 10 mas with even a few of them up to tens of mas. Some sources with small position uncertainties show large angular differences, which also happens in the Gaia DR2 sources when compared with the ICRF3 prototype.

### 6.2. Systematics analysis

The alignment of the optical positions in Gaia DR2 with respect to the ICRF2 can be modelled by an infinitesimal solid rotation with the following equations (Lindgren (2016)):

$$\begin{aligned} \Delta\alpha_* &= -\epsilon_X \cos \alpha \sin \delta - \epsilon_Y \sin \alpha \sin \delta + \epsilon_Z \cos \delta \\ \Delta\delta &= +\epsilon_X \sin \alpha - \epsilon_Y \cos \alpha \end{aligned} \quad (8)$$

Where  $\Delta\alpha_* = \Delta\alpha \cos \delta$ .  $\epsilon_X$ ,  $\epsilon_Y$  and  $\epsilon_Z$  are the three rotation angles around the ICRS parameters.

**Table 4.** Global difference between the Gaia-CRF2 positions of ICRF sources and their positions in ICRF2.

Source subset	N	$\epsilon_x$ ( $\mu$ as)	$\epsilon_y$ ( $\mu$ as)	$\epsilon_z$ ( $\mu$ as)
All	1321	$115 \pm 108$	$46 \pm 105$	$-56 \pm 195$
Defining	139	$184 \pm 72$	$-58 \pm 72$	$-13 \pm 132$
Non-defining	1182	$82 \pm 124$	$-14 \pm 120$	$-45 \pm 133$

The weighted least-squares estimation of the orientation parameters between Gaia-CRF2 and ICRF2 are listed in table 4. No significant rotation is found at the level of  $0.1 \text{ mas}$ .

## 7. Conclusions

We analysis the properties of the QSOs astrometric solutions of 779349 QSOs (indicated as KQCG) from the known QSOs sample, which is about 40% more than the Gaia-CRF2 QSOs sample, the conclusions are as follows:

1. The mean global parallaxes bias for the KQCG quasars sample is  $-0.0308 \text{ mas}$  and the median value is  $-0.0283 \text{ mas}$ , which agrees with the results in the Gaia DR2 paper. The roughly quadratic variation with  $\sim 0.010 \text{ mas}$  smaller parallaxes towards the ecliptic poles is most likely caused by the fainter sources around the ecliptic poles.
2. The VSH method is applied to the proper motion vector field of different QSOs sample. The rotation result of KQCG agrees with the result of Type2+Type3 quasars sample. The GCRF2 quasars sample result shows a very different rotation with respect to KQCG. The rotations of them are not larger than  $10 \mu\text{as/yr}$  for each axis. The glide vector of KQCG is about  $(-8.7, +9.6, +8.9) \pm 2.7 \mu\text{as/yr}$ . The Type2+Type3 sample shows a different rotation in northern and southern hemisphere. While the rotation of the KQCG sample agrees in northern and southern hemisphere in  $x$  and  $y$  components.
3. There is a  $\sim +0.01 \text{ mas/yr}$  bias in the declination direction of proper motion, and the typical glide of the proper motion field is  $(-9, 8, 0) \pm 2 \mu\text{as/yr}$  after subtracting the bias in  $\mu_\delta$ .
4. The scalar harmonics sphere expansion of the parallaxes show a significant harmonic degree at  $l=4$  with significance of  $Z_{\chi^2} \sim 7$ .
5. The ICRF2 sources are cross matched with the Gaia DR2 sources. Only the sources in the northern hemisphere are found, which may caused by the generally substantially worse position errors in southern hemisphere. The systematic between the ICRF2 sources and the corresponding Gaia DR2 sources is analyzed, no significant rotation signal is found.

**Acknowledgements.** This work has made used of data from ESA space mission Gaia, processed by the Gaia Data Processing and Analysis Consortium (DPAC). We are grateful to the developers of the TOPCAT (Taylor (2005)) software. Guoshoujing Telescope (the Large Sky Area Multi-Object Fiber Spectroscopic Telescope LAMOST) is a National Major Scientific Project built by the Chinese Academy of Sciences. Funding for the project has been provided by the National Development and Reform Commission. LAMOST is operated and managed by the National Astronomical Observatories, Chinese Academy of Sciences. This work has been supported by the grants from the National Science Foundation of China (NSFC) through grants 11703065 and 11573054.

## References

- Bolton A S, Schlegel D J, Aubourg É, et al. Spectral classification and redshift measurement for the SDSS-III baryon oscillation spectroscopic survey[J]. The Astronomical Journal, 2012, 144(5): 144.
- Bucciarelli B, Abbas U, Vecchiato A, et al. Comparison of two Gaia sphere solutions using orthonormal bases on the sphere
- Croom S M, Smith R J, Boyle B J, et al. The 2dF QSO Redshift Survey–XII. The spectroscopic catalogue and luminosity function[J]. Monthly Notices of the Royal Astronomical Society, 2004, 349(4): 1397-1418.
- Cui, X. Q., Zhao, Y. H., Chu, Y. Q., et al. 2012, Research in Astronomy and Astrophysics, 12, 1197
- Eisenstein D. The Baryon Oscillation Spectroscopic Survey (BOSS): Dark Energy from the World’s Largest Redshift Survey[C]//APS April Meeting Abstracts. 2015.
- Fey A L, Gordon D, Jacobs C S, et al. The second realization of the international celestial reference frame by very long baseline interferometry[J]. The Astronomical Journal, 2015, 150(2): 58.
- Hewitt A, Burbidge G. A revised and updated catalog of quasi-stellar objects[J]. The Astrophysical Journal Supplement Series, 1993, 87: 451-947.
- Liao S., Qi Z., et al. A compilation of known QSOs for the Gaia mission[J]. arXiv preprint arXiv:1804.08821, 2018.
- Lindgren L, Lammers U, Bastian U, et al. Gaia Data Release 1: Astrometry - one billion positions, two million proper motions and parallaxes[J]. Astronomy & Astrophysics, 2016, 595.
- Lindgren L, Hernandez J, Bombrun A, et al. Gaia Data Release 2: The astrometric solution[J]. arXiv preprint arXiv:1804.09366, 2018.
- Malkin Z, Jacobs C S, Arias F, et al. The ICRF-3: Status, plans, and progress on the next generation International Celestial Reference Frame[J]. arXiv preprint arXiv:1511.08035, 2015.
- Mignard F, Klioner S. Analysis of astrometric catalogues with vector spherical harmonics[J]. Astronomy and Astrophysics, 2012, 547: A59.
- Mignard F, Klioner S, Lindgren L, et al. Gaia Data Release 2: The Celestial reference frame (Gaia-CRF2)[J]. arXiv preprint arXiv:1804.09377, 2018.
- Pâris I, Petitjean P, Aubourg É, et al. The Sloan Digital Sky Survey quasar catalog: tenth data release[J]. Astronomy & Astrophysics, 2014, 563: A54.
- Pâris I, Petitjean P, Aubourg E, et al. The Sloan Digital Sky Survey Quasar Catalog: Fourteenth Data Release[J]. arXiv preprint arXiv:1712.05029, 2017.
- Secrest N J, Dudik R P, Dorland B N, et al. Identification of 1.4 Million Active Galactic Nuclei in the Mid-Infrared using WISE Data[J]. The Astrophysical Journal Supplement Series, 2015, 221(1): 12.
- Souchay, J., Andrei, A. H., Barache, C., et al. 2015, Astronomy and Astrophysics, 583
- Taylor M B, Shopbell P, Britton M, et al. ASP Conf. Ser. Vol. 347, Astronomical Data Analysis Software and Systems XIV[J]. 2005.
- Véron-Cetty M P, Véron P. A catalogue of quasars and active nuclei[J]. Astronomy & Astrophysics, 2010, 518: A10.